ACS OMEGA

http://pubs.acs.org/journal/acsodf

Article

Analysis of Crystallographic Structures and Properties of Silver Nanoparticles Synthesized Using PKL Extract and Nanoscale Characterization Techniques

Md. Hazrat Ali,* Md. Abul Kalam Azad, K. A. Khan, Md. Obaidur Rahman, Unesco Chakma, and Ajoy Kumer*

Cite This: *ACS Omega* 2023, 8, 28133−28142

Read Online

ACCESS | Metrics & More | Article Recommendations | Supporting Information

ABSTRACT: In this cutting-edge research era, silver nanoparticles impose a substantial impact because of their wide applicability in the field of engineering, science, and industry. Regarding the vast applications of silver nanoparticles, in this study, the crystallographic characteristics and nanostructures of silver nanoparticles extracted from natural resources have been studied. First, biosynthetic silver nanoparticles were synthesized using the Pathor Kuchi leaf (PKL) extract as a mediator, and their crystal structures and characteristics were analyzed by UV−visible absorption spectroscopy, Fourier transform infrared (FTIR) spectroscopy, X-ray diffraction (XRD), field-emission scanning electron microscopy (FESEM), and energy-dispersive X-ray (EDX) analysis. The average crystallite size of the synthesized silver nanoparticle was determined to be 20.26 nm, and also the lattice strain, intrinsic stress, and dislocation density were measured to be 2.19×10^{-3}, 0.08235 GPa, and 3.062045×10^{-3}/nm^2, respectively. Further, the prepared sample of silver nanoparticles shows four peaks in the X-ray diffraction pattern, which correspond to the (111), (200), (220), and (311) face-centered cubic (FCC) crystalline planes. The outstanding finding of this work was that when the lattice parameters of the precursor were increased, the volume of the material did not considerably change, but the particle size decreased. Second, it was clearly demonstrated that this straightforward method is a clean, cost-effective, environmentally sustainable, nontoxic, and efficient route for the synthesis of silver nanoparticles (Ag NPs) using PKL leaf at ambient temperature, which also satisfies the green chemistry requirements. Finally, this study demonstrates the scope for the production of silver nanoparticles using low-cost natural resources.

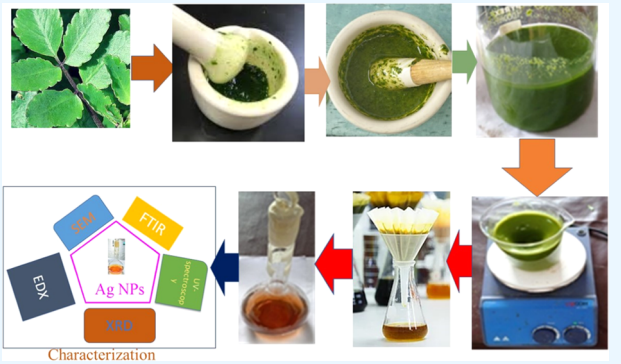

1. INTRODUCTION

The use of nanomaterials and nanotechnology in the advancement of science and technology is preferable for modern researchers around the world. Moreover, nanoparticles play a significant role in the creation of environmentally sustainable and robust future technology for human beings, including the scope for green chemistry. Among the different forms of nanoparticles, metal-based nanoparticles are highly desired for their wide range of applicability. First and foremost, one of the most significant areas for researchers[1,2] is the production or synthesis of metal nanoparticles and the expansion of their many applications in the manufacturing, biomedical engineering, biological synthesis, and pharmaceutical sectors. Particles with a size in the nanoscale range of 1−100 nm are called nanoparticles.[1,2] The nanoparticle behavior might differ significantly from that of the bulk form when particles are shrunk in size. Nanoparticles have been employed in several fields, including medicine, semiconductors, catalysis, electrolysis, optoelectronic materials, and the energy sector, recently. In particular, silver nanoparticles have been developed for use in a range of therapeutic applications (including antimicrobial, anti-diabetic, anti-cancer, anti-parasitic, and antioxidant), biomolecular diagnostics, medicine, textile-manufacturing facilities, dental implant raw materials, and water purification systems.[3−7] In addition, it must be noted that these materials are also utilized in the advancement of nanoparticles (NPs) in areas such as producing clean energy, catalysis, solid-state electronic components, and sensor or biosensor manufacture, among others.[8,9] The capacity to reliably use these materials offers opportunities for the development of nanoparticles (NPs) in these areas. Currently, research is ongoing for materials for applications in the

Received: February 24, 2023
Accepted: July 6, 2023
Published: July 28, 2023

© 2023 The Authors. Published by American Chemical Society

Figure 1. Flow diagram of the juice or extract preparation from PKL.

biological sector as a reducing agent of proteins and metabolites in many biological systems, such as plants and algae,[10] diatoms,[11,12] bacteria,[13] yeast,[14] fungi,[15] and human cells.[16] In addition, the extraordinary optical[17] and chemical[18] characteristics of metallic nanoparticles make their biological synthesis extremely alluring. On the other hand, flavonoids and proteins extracted from the Pathor Kuchi leaf (PKL) are highly applicable as reducing agents of biochemical reactions. Furthermore, PKL is widely accepted and appreciated for its medicinal effectiveness against antiviral and antibacterial outbreaks.[19] PKL also allows the flexible synthesis of various metal-based nanoparticles, which will have various applications in pharmaceutical inhibitors, catalytic materials, and materials for optoelectronics devices. Especially in the last decade, PKL has been highly used in the area of electrochemistry for producing materials with voltage regulation, capacity, and energy efficiency, as well as for enhancing the performance of existing materials. Therefore, we were motivated and attempted to investigate synthetic techniques for nanoparticles from PKL that have the potential to open a new dimension for numerous applications in the above-mentioned areas. However, inorganic metal ions in metal nanoparticles play a vital role in their properties and applications, so that the surface area of a particle drastically increases in its size. This makes it possible for novel optical characteristics to emerge, and also enhanced electrical and thermal conductivities, lowered melting point, increased magnetism, and other properties can all result from this phenomenon.[20] A variety of plant extracts have been successfully used for the efficient and rapid extracellular synthesis of gold and silver nanoparticles, including geranium (*Pelargonium graveolens*),[21] lemongrass (*Cymbopogon flexuosus*),[22] cinnamon (*Cinnamomum camphora*),[23] neem (*Azadirachta indica*),[24] aloe vera (*Aloe vera*),[25] tamarind (*Tamarindus indica*),[26] and the fruit extract of Emblica officinalis.[27] The production and association of metallic nanoparticles[28,29] would benefit from "green chemistry" procedures that are safe, nontoxic, and environmentally acceptable, perhaps utilizing bacteria, fungi, or even plants. It is well established[30,31] that the shape and nanostructure size of metal NPs, particularly Ag NPs, are influenced by their functional characteristics. Nanoparticles, due to their exceedingly small size, huge surface area, optical scattering, and fluorescence, have potential biomedical applications.[32]

Furthermore, due to the high price of gold, silver is a more user-friendly material for the synthesis of nanoparticles from natural resources, despite the fact that it has numerous applications in several fields and new materials are being constantly discovered. Ag nanoparticles can be synthesized by many effective methods, for example, chemical reduction, green synthesis, laser ablation, γ irradiation, electron irradiation, chemical and photochemical techniques, microwave processing, and biological synthetic processes. Among them, green synthesis methods can be considered the most sustainable and cost-effective methods for synthesizing nanoparticles from natural sources by using plants or microorganisms. Moreover, it helps to produce nanoparticles using a wide variety of physical, chemical, biological, and hybrid approaches.[33−36] In this study, the Pathor Kuchi leaf (PKL) extract was chosen for the green synthesis of Ag nanoparticles. Here, a green synthesis technique is used to produce silver nanoparticles from silver nitrate salt. Crystallographic characteristics and structures of silver nanoparticles depend heavily on bioreducers; hence, it is extremely crucial to characterize these materials structurally. Herein, we show comprehensive results using various characterization techniques (UV−vis, FTIR, XRD, FESEM, and EDX) on silver nanoparticles synthesized using the Pathor Kuchi leaf (PKL) extract, including crystal structure and characteristics measured on the nanoscale and the significance of their microstructure features.

2. METHODS AND MATERIALS

2.1. Raw Materials and Reagents. Reagents and raw materials utilized in this investigation did not require any special purification procedures because of their outstanding analytical quality. For this study, deionized water with a resistivity of 18 Ω·m was used to prepare the silver nitrate ($AgNO_3$) solution. The materials and reagents utilized in this experiment were as follows: Whatman filter papers 41 and 42, distilled water, deionized water, solid silver nitrate ($AgNO_3$), Pathor Kuchi leaves, and PKL extract.

2.2. Apparatus and Auxiliaries. The following devices and auxiliaries (shown in Figure S1a−d) were used to create silver nanoparticles (Ag NPs): rotating magnetic stirrer plate (Labcom, MS-1003; heat range: 0−340 °C; revolution: 0−

https://doi.org/10.1021/acsomega.3c01261
ACS Omega 2023, 8, 28133−28142

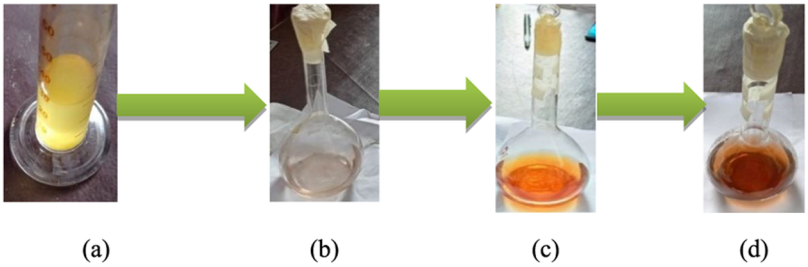

Figure 2. Color change scenario of silver nanoparticle formation: (a) PKL extract; (b) raw silver nitrate solution (3 mM) and filtered PKL juice mixture, colorless at the beginning; (c) light-orange (yellowish) color after 30 min; (d) brown color with some black sediment after 45 min.

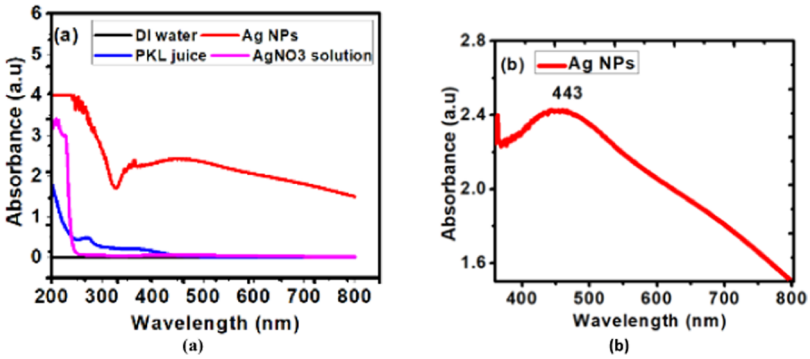

Figure 3. UV−visible spectra of (a) different samples and (b) Ag NPs in the liquid form.

4000 rpm), centrifuge machine (800 Centrifuge, China; revolution: 0−4000 rpm), refrigerator, blender machine, volumetric flux, measuring flux, conical flux, calibrated beaker, magnet bar, sample holder, thermometer, glass vial, etc.

2.3. Equipment Used for Characterization. The following tools were used for different levels of characterizations of silver nanoparticles (Ag NPs): a UV−visible Spectrometer (UV-1800, 240 V, Shimadzu, double-beam spectrometer, made in Japan; Figure 2Sa), a Fourier transform infrared spectrophotometer (IR Prestige-21 Kyoto, made in Japan; Figure 2Sb), an X-ray diffractometer (Rigaku Ultima IV, made in Japan; Figure 2Sc), and a field-emission scanning electron microscope (FESEM) (Jeol JSM-7600F field-emission SEM; Figure 2Sd).

2.4. Preparation of the PKL Sap and PKL Extract. From a local nursery, fresh Pathor Kuchi leaves (PKL) were obtained. The gathered leaves were gently cleaned to get rid of dust and impurities. Multiple washes with both regular and deionized water were performed to thoroughly remove all traces of dust, and the item was dried under a ceiling fan at room temperature (28−29 °C) to ensure that no moisture was left behind. The leaves were then placed in a beaker after being crushed with a blending machine. 20 g of PKL paste was combined with 100 mL of deionized water using a magnetic stirrer and a 60 °C hot plate.[37,38]

After allowing the mixture (PKL paste and deionized (DI) water) to cool down to room temperature, the PKL extract was obtained by filtering it twice using Whatman 41 and Whatman 42 filter papers. The full procedure is presented in Figure 1a−h.

2.5. Synthesis of Silver Nanoparticles (Ag NPs). Using a straightforward green synthesis approach, silver nitrate ($AgNO_3$) salt was employed as a precursor, while the PKL extract was used as an excellent source of reducing and capping agents. Ultrapure analytical-grade $AgNO_3$ from Sigma Aldrich was used as a precursor in this experiment. The whole preparation of silver nanoparticles was carried out by slowly adding 10 mL of filtered PKL extract dropwise with 90 mL of 3 mM $AgNO_3$ solution in a conical flux, as depicted in Figure 2a−d.

The mixture was then stored in a dark place for future observation and examination. The formation of Ag NPs was confirmed by a change in the color from completely colorless to light orange (yellowish) in 30 min and then from light orange to brown, with some black sediment at the bottom of the conical flask after 45 min. Images showing the change in colors are displayed in Figure 2. The silver nanoparticle colloidal solution was then dried using a centrifuge (800 Centrifuge, China: revolution: 0−4000 rpm) and a magnetic stirrer equipped with a hot plate (Labcom, MS-1003: heat range: 0−340 °C; revolution: 0−1500 rpm) was used to produce powdered samples for subsequent sequential probing.

2.6. Characterizing Green-Synthesized Silver Nanoparticles Mediated by the PKL Extract. A UV−visible spectrometer (UV-1800, 240 V, Shimadzu, a double-beam spectrometer made in Japan) was used to observe and inspect the green-synthesized silver nanoparticles, and the spectra of the reaction solution were measured (3 times diluted) in the range of 200−800 nm. Using a Shimadzu IR Prestige-21 FT-IR spectrophotometer, the attenuated total reflection Fourier transform infrared (ATR/FTIR) spectra of the PKL extract and silver nanoparticles (powder form) mediated by the PKL extract were carefully recorded. A Rigaku Ultima IV, a Japanese X-ray diffraction device, was used to probe the crystalline phase and structure of Ag NPs. XRD measurements were performed from 10 to 80° at 2θ angles using Cu Kα radiation (λ = 1.54056 Å). All of these tests were carried out at the University of Dhaka's Centre for Advanced Research in Sciences (CARS). The morphology of silver nanoparticles was investigated using a field-emission scanning electron

https://doi.org/10.1021/acsomega.3c01261
ACS Omega 2023, 8, 28133−28142

microscope (FESEM) (Jeol; JSM-7600) re-equipped with an energy-dispersive X-ray (EDX) spectrometer at 15 keV at the Nano lab, Glass and Ceramics Institute of BUET. To prepare the sample for FESEM imaging, Ag NPs were placed in a JEC-3000FC auto fine platinum coater for 10 s.[33]

3. RESULTS AND DISCUSSION

3.1. Formation of Silver Nanoparticles by UV−Visible and FTIR Spectroscopies. The color-changing scenario (from light-yellow to brown) of the silver nitrate and PKL extract solutions (Figure 2a−d) allows one to discern the production of silver nanoparticles mediated by the Pathor Kuchi leaf extract. At certain time intervals after adding the PKL extract into the $AgNO_3$ solution, the silver ions (Ag^+) are bioreduced into silver nanoparticles Ag^0(Ag NPs), as observed by the color change. This is the first sign that silver nanoparticles (Ag NPs) are being formed. The formation of silver nanoparticles is depicted in Figure 2 by a range of colors changing from yellow to brown.[39,40] In addition, Figure 3a,b displays the UV−visible spectra of various samples.

Surface plasmon resonance (SPR) causes Ag NPs to absorb light differently depending on their size, with the strongest effect observed between 400 and 500 nm.[41] Further, lower band absorption indicates a smaller particle size, while higher band absorption is compatible with larger nanoparticles.[42] Upon exposing silver nanoparticles to light, free electrons in them vibrate, causing an absorption band characteristic of surface plasmon resonance to develop.[43] The size, shape, morphology, solvent type, and concentration all affect the wavelength range in which Ag NPs radiate.[44,45] Absorption maxima are studied, and the highest peak is observed at about 443 nm. The black line indicates the peak of the reference solvent; therefore, it does not represent any specific peak. Moreover, $AgNO_3$ solution (magenta line) was utilized as a precursor of Ag, which is comparable to the peak of Ag NPs, represented by a red-colored line. It is worth noting that no peaks attributable to DI water, $AgNO_3$ solution, and PKL juice are visible; however, Ag NPs demonstrate a peak in 443 nm. Surface plasmon absorption of silver nanoparticles, as depicted in Figure 3a, results from the reduction of Ag^+ to Ag^0.

Second, Ag NPs contain various functional groups, such as amino, alkyne, amide, ketone, nitro, ester, etc. The FTIR spectra of the filtered PKL extract show several peaks at 3383.14 cm^{-1} (N−H stretch), 2320.37 cm^{-1} (C≡N; alkynes: 2300−2200 cm^{-1}), 2117.84 cm^{-1} (C≡C; alkynes: 2200−2100 cm^{-1}), 1639.49 cm^{-1} (C═O, amide I band; ketones: 1750−1625 cm^{-1}; C═O stretch), 1388.75 cm^{-1} (N═O; nitro groups: 1400−1300 cm^{-1}), and 1274.95 cm^{-1} (−O stretch; ethers: 1300−1000 cm^{-1}) positions. The presence of flavonoids in the water-soluble plant extract may have caused the reduction of Ag^+ to Ag^0 in the $AgNO_3$ solution. Several peaks were observed at 480.28, 825.53, 881.47, 1080.14, 1384.89, 1581.63, 1712.79, 2927.94, 3435.22, 3697.54, and 3755.40 cm^{-1} in the spectrum.

3.2. Analyzing the Nanostructure of Ag NPs Using Crystallographic X-ray Diffraction Data. XRD measurements were performed in the Bragg−Brentano geometry to investigate the crystal nanostructure of the above-mentioned silver nanoparticles (Ag NPs). The XRD equipment was used to analyze Ag NP powder samples. The XRD pattern (diffractogram) of Ag NPs, indexed in origin pro software, is displayed in Figure 4.

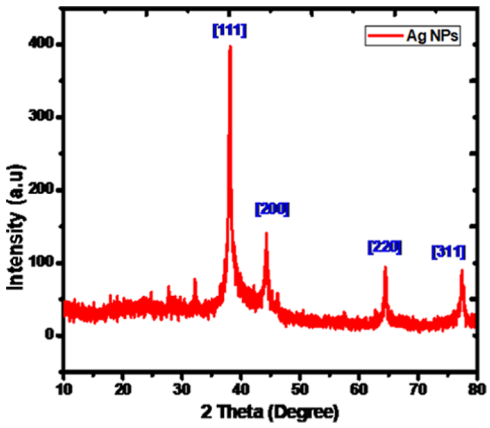

Figure 4. XRD pattern of green-synthesized silver nanoparticles (Ag NPs).

In the XRD pattern, diffraction peaks were seen around 38.070, 44.290, 64.440, and 77.340 positions. According to the crystallographic lattice planes, the indexed and Miller Indices (*hkl*) for each peak are (111), (200), (220), and (311) (Ref: Joint Committee on Powder Diffraction Standards, JCPDS file No. 04-0783). The highly intense peak demonstrates the polycrystalline phase composition of the produced silver nanoparticles, confirming the synthesis of face-centered cubic (FCC) crystalline silver nanoparticles. The production of silver nanoparticles of a larger size is evident from the observation that their diffraction profiles are broadened in comparison to those of bulk silver. The standard diffraction angles (2θ) and the experimental diffraction angles (2θ) in Table S2 also agree well.[46−48]

In addition, ratios of (200)/(111) and (220)/(111) diffraction peak intensities presented in Table S3 are slightly lower than the established values (0.26 vs 0.31 and 0.19 vs 0.22).[49]

3.3. Crystallite Size, Interplanar *d*-Spacing, and Lattice Parameters of Silver Nanoparticles. Figure 4 displays the X-ray diffraction pattern produced by the as-prepared silver nanoparticles. Reflections from the (111), (200), (220), and (311) lattice planes of FCC silver nanoparticles can be seen as a series of intense Bragg reflections. All of the reflections are consistent with the crystalline structure of silver metal with a face-centered cubic symmetry. The sample exhibits the expected highly intense (111) reflection, which is indeed typical for FCC materials. The high degree of crystallinity of silver nanoparticles is evident in the intensity of peak position reflections. A modest crystallite size is indicated by the large diffraction peaks.[50] The XRD analysis confirms the crystalline nature of the silver nanoparticles. The crystallite size of silver nanoparticles was determined to be 20.26 nm using the Debye−Scherrer eq 1[51−53]

$$D = \frac{0.89\lambda}{\beta \cos\theta} \quad (1)$$

where the Cu Kα X-ray wavelength λ = 0.154056 nm, θ is Bragg's diffraction angle (° or radian), β (radian) is the full width at half-maximum (FWHM) of the maximum intensity peak, and 2θ = 38.07°, as shown in Table S1. Table 1 shows that the average crystallite size of the green-synthesized Ag NPs is 21.65 nm, based on data from XRD analysis. Bragg's

https://doi.org/10.1021/acsomega.3c01261
ACS Omega 2023, 8, 28133−28142

Table 1. Data of Crystallite Diameter Size, Interplanar Spacing, and Lattice Parameters of the Prepared Silver Nanoparticles

2θ of the intense peak (°)	FWHM β (°)	Miller indices (hkl)	crystallite diameter D (nm)	interplanar spacing, d (nm)	lattice parameters (a) nm
38.07	0.41	111	21.4	0.2361	0.4089
44.29	0.64	200	14.1	0.2043	0.4086
64.44	0.35	220	27.9	0.1444	0.4084
77.34	0.46	311	23.2	0.1232	0.4086
average values (nm)			21.65	0.1770	0.4086

Law[46] is applied to several atomic planes to determine its interplanar separation or d by eq 2.

$$2d\sin\theta = n\lambda \tag{2}$$

Here, d is indicated by the interplanar spaces. The lattice parameter for each peak position[46] is calculated using eq 3.

$$\frac{1}{d^2} = \frac{(h^2 + k^2 + l^2)}{a^2} \tag{3}$$

Each peak lattice value is listed in Table 1, where the average lattice parameter is 0.4086 nm. The resulting lattice parameters are considerably close to the lattice parameter of silver nanoparticles, JCPDS file number 04-0783 (a = 0.4086 nm).

3.4. Lattice Crystal Planes of the XRD Data Obtained from the XRD Diffractogram. Lattice planes are typically designated by using Miller Indices. Silver nanoparticles used in this work were analyzed by an XRD diffractometer, and the lattice planes were identified, which are shown in Figure S3.

3.5. Radius Calculation of the Prepared Ag NPs. The produced silver nanoparticles have an FCC crystal structure, with a unit cell edge, a = 4.086 Å. Using eq 4, we can determine the radius (r) of the silver nanoparticles, and we find r = 0.144 nm for the manufactured silver nanoparticles.

$$a = \frac{4r}{\sqrt{2}} \tag{4}$$

3.6. Volume and Atomic Packing Factor (APF) Calculation. In the case of a hard spherical model, the packing factor is the ratio of the total volume of atomic spheres to the volume of a unit cell. Both eqs 5 and 6 can be used to determine the volume V_S and unit cell volume V_C of the 4 atoms in the FCC crystal structure.

$$V_S = 4 \times \frac{4}{3}\pi R^3 \tag{5}$$

$$V_C = a^3 = \left(\frac{4R}{\sqrt{2}}\right)^3 = 16R^3\sqrt{2} \tag{6}$$

Here, R = 0.144 nm and the FCC unit cell has 4 atoms.

$V_S = 4 \times \frac{4}{3}\pi(0.144)^3 = 0.050030\ \text{nm}^3$, $V_C = 16(0.144)^3(\sqrt{2}) = 0.067565\ \text{nm}^3$, APF $= \frac{0.05003}{0.067565} = 0.74 = 74\%$. The atomic packing factor indicates that atoms are tightly bonded or tightly packed in the lattice structure. These values are given in Table 3.

3.7. Surface Area-to-Volume Ratio Calculation.

$$\text{surface area of Ag NPs, } SA_{part} = 4\pi R^2 \tag{7}$$

$$\text{volume of particle, } V_{part} = \frac{4}{3}\pi R^3 \tag{8}$$

The synthesized Ag NPs were measured to have a surface area of 1289.50 nm^2 = 1289.5 × 10^{-18} m^2 and a volume of 4354.28 nm^3 = 4354.28 × 10^{-27} m^3; the surface area-to-volume ratio is 29.6 × 10^7, which is significantly larger. The rate at which a chemical reaction occurs is directly related to the surface area of a solid, measured as the ratio of its surface area to its volume (SA/V) or its specific surface area (SSA). As there are enough potential surfaces to react, materials having a high SA/V (extremely small diameter) exhibit substantially faster reaction times compared to monolithic materials.

3.8. Analysis of Strain in a Lattice. Non-uniformities in the lattice, such as faulting, dislocations, antiphase domain borders, and grain surface relaxation all contribute to the lattice strain, as shown in Table 2. Using the Williamson–Hall eq 9,[54−56] we may determine the crystallite size and lattice strain. Peak broadening in the diffraction pattern because of experimental errors can be calculated using the following formula.

$$\beta\cos\theta = \frac{0.89}{D} + 4\varepsilon\sin\theta \tag{9}$$

where β is the full width at half-maximum, ε is the lattice strain, D is the average crystallite size, θ is Bragg's diffraction angle, and the radiation wavelength λ = 0.154056 nm. Instrumental errors, particle size reduction, strain, etc., can all likely to lead to a significant broadening of diffraction peaks, as seen in ref 57, 58.[57,58]

Here, the Williamson–Hall graph is plotted with 4 sin θ on the x-axis and $\beta\cos\theta$ on the y-axis (β in radians). The particle size and strain can be calculated using the y-intercept and slope of the linear fit line, respectively. The extracted particle size of the manufactured silver nanoparticles was determined to be 12.32 nm, and its lattice strain was determined to be 2.19 × 10^{-3}. The Williamson–Hall plot for the green-synthesized Ag nanoparticles is displayed in Figure 5.

3.9. Calculating Intrinsic Stress (σ_S). We utilized eq 10[59,60] to compute the intrinsic stress created in the nanoparticles due to the departure of the observed lattice constant of silver nanoparticles from the bulk.

$$\sigma_S = \frac{Y(a - a_0)}{2a_0\gamma} \tag{10}$$

For silver, Young's modulus Y = 83 GPa, a = 0.4089 nm for the lattice constant, a_0 = 0.4086 nm for the bulk lattice constant,

Table 2. Williamson–Hall Plotting Data

2θ of the intense peak (°)	FWHM β (°)	FWHM β (radians)	cos θ	$\beta\cos\theta$	4 sin θ	diameter size D (nm)	lattice strain
38.07	0.41	0.007155849	0.94531952	0.00676456	1.30458271		
44.29	0.64	0.011170107	0.92623285	0.01034612	1.50780736	12.23	2.19 × 10^{-3}
64.44	0.35	0.006108652	0.84600710	0.00516796	2.13268648		
77.34	0.46	0.008025145	0.78075767	0.00626569	2.49933572		

https://doi.org/10.1021/acsomega.3c01261
ACS Omega 2023, 8, 28133−28142

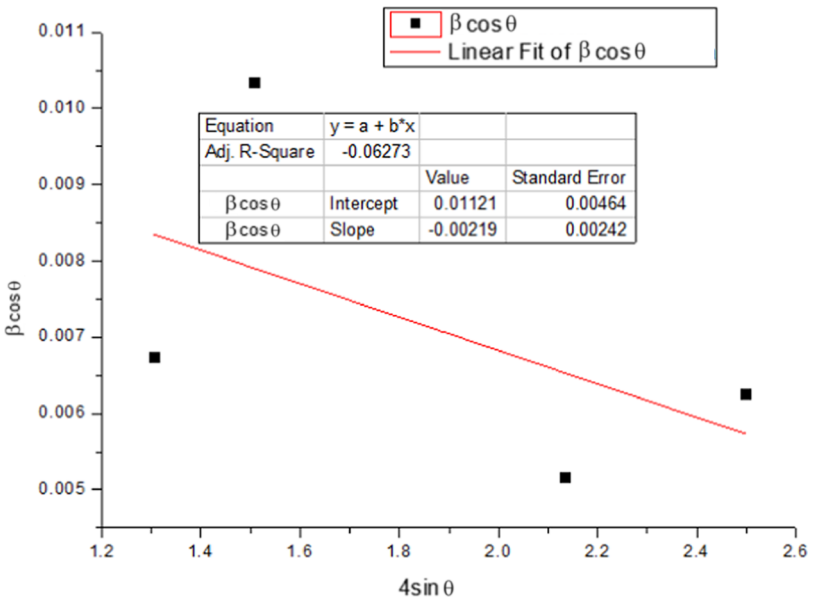

Figure 5. Williamson–Hall plot of the prepared silver nanoparticles.

Table 3. Some Structural and Mechanical Properties

lattice strain (ε)	intrinsic stress (σ_S) (GPa)	dislocation density (δ) (m^2)	specific surface area (S) (m^2/g)	atomic sphere volume (nm^3)	volume of unit cell (V_C) (nm^3)	APF
2.19×10^{-3}	0.08235	3.062045×10^{-3}	28.2	0.050030	0.067565	0.74

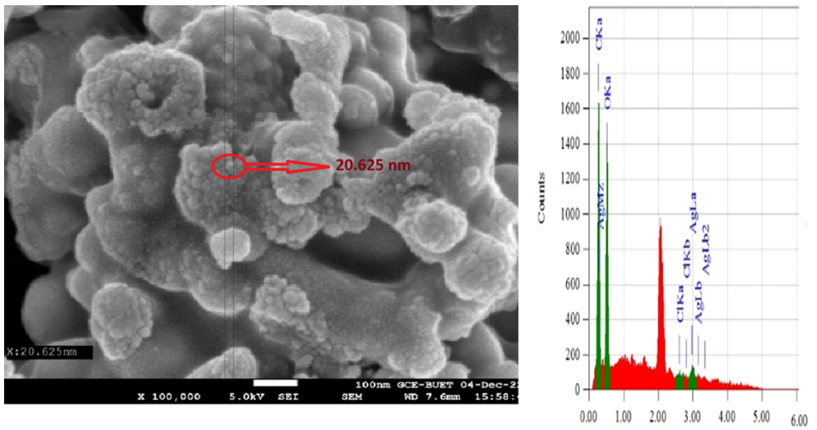

Figure 6. (a) FESEM image of the prepared Ag nanoparticles. (b) EDX spectrum.

and $\gamma = 0.37$ for the Poisson's ratio. The intrinsic stress of the sample was measured to be 0.08235 GPa.

3.10. Calculation of the Dislocation Density (δ). The magnitude of crystal defects is represented by the dislocation density value, which is the number of dislocation lines per unit volume of the crystal. The degree of crystallinity of nanoparticles can be described by the dislocation density value. Using expression 11,[61] the dislocation density in the nanoparticles has been calculated as follows.

$$\delta = \frac{15\beta \cos\theta}{4aD} \tag{11}$$

$D = 20.26$ nm, $a = 0.4089$ nm, and β = FWHM. For many material properties, the existence of dislocations is an apex-determining factor.[54] Such defects distort the regular atomic array of a perfect crystal structure. The value of 3.062045×10^{-3} $1/nm^2$ was determined to be extremely small. The high crystallinity of the silver nanoparticles that were generated in this way is indicated by the low dislocation density value.[62]

3.11. Calculation of the Specific Surface Area (S). The specific surface area is particularly relevant to nanomaterials because as the particle size reduces, the specific surface area increases. This is especially significant for surface reactions, heterogeneous catalysis, and adsorption. The specific surface area of a material decreases as its particle size increases, making particle size a decisive element to consider when working with nanomaterials. The Brunauer–Emmett–Teller (BET) eq 12 can be used to determine the specific surface area.[63−65]

$$S = \frac{6 \times 10^3}{D_P \times \rho} \tag{12}$$

The nanoparticle size is denoted as D_p, the density of silver is assumed to be 10.5 g cm^{-3}, and S denotes the specific surface area. The surface area per gram of the produced silver

https://doi.org/10.1021/acsomega.3c01261
ACS Omega 2023, 8, 28133−28142

nanoparticles was determined to be at 28.2 m^2, as presented in Table 3.

3.12. Calculation of the Crystalline Index. The original crystallite size of a nanomaterial is proportional to the peak width of the phase of that nanomaterial. A more pronounced peak in the XRD pattern is indicative of a crystal material. Peak broadening was found in the XRD data collected from silver nanoparticles. The particle size was measured to be 20.26 nm using the Debye−Scherrer equation, while the crystallite size was determined to be 20.62 nm using the FESEM particle size standard. Therefore, we may now assess the crystallinity of the sample with an index of 1.018 (≥1.00).[66] Eq 13 for the crystalline index calculation is given below

$$I_{cry} = \frac{D_p(\text{SEM, TEM})}{D_{cry}(\text{XRD})} \ (I_{cry} \geq 1.00) \tag{13}$$

where I_{cry} is the crystallinity index, D_p is the particle size obtained from the FESEM image (shown in Figure 6a), and D_{cry} is the particle size (calculated from the Debye−Scherrer equation).

3.13. Data Analysis Using a Field-Emission Scanning Electron Microscope and an Energy-Dispersive X-ray Spectrometer. Silver nanoparticles of varying sizes and shapes were examined using FESEM to learn more about nanostructured materials. Silver nanoparticles produced using the PKL extract are illustrated in Figure 6a,b.

The results demonstrated the wide range of sizes and shapes of the silver nanoparticles. In comparison to pure silver, these substances could have some sort of unusual properties. Characteristics such as a large specific surface area, high surface reaction, and a well-organized transmission channel for the analyte molecules to reach the active sites will help develop stability and sensitivity of silver nanoparticles, and hence, Ag nanoparticles show outstanding current sensitivity for both hydrogen peroxide (H_2O_2) and dopamine (DA). It is also revealed that the overall crystal form is spherical in shape. From the FESEM images, the sample grain sizes were estimated to be 20.62 nm. The size of polycrystalline particles is depicted by the FESEM image. Most metals, including Ag, have FCC structures and grow from nucleation into twinned and multiply twinned particles (MTPs) with surfaces bordered by the lowest-energy (111) facets. Ag nanoparticles tend to agglomerate due to the high surface energy and high surface tension of the ultrafine nanoparticles, which may account for the observation of some larger nanoparticles. Catalytic activity, a crucial feature of the produced Ag NPs, is enhanced by their small particle size and wide surface area.[67]

Figure 6b shows the EDX spectra of the produced Ag nanoparticles. The sample was analyzed for its elemental composition using an EDX spectrometer attached to a field-emission scanning electron microscope.

Here, L and K are indicated by the first and second shells of the orbit for any atom. In the case of Ag atoms, the first shell represents AgL, where the electron transition or emission occurs due to the X-ray peak. In addition, the upper peak is called α (α) and the lower peak is called β (β). Now, AgLα, AgLβ, and AgLβ2 are the emissions from M to L, from N to L, and from the second subshell of N to L. Similarly, CKα indicates electron transition from the L to K shell of the carbon atom; OKα indicates L to K shell electron transition of the oxygen atom, and ClKα indicates the L to K shell electron transition of the chlorine atom. Binding energy peaks at 3.0, 3.2, and 3.3 keV are associated with AgLα, AgLβ and AgLβ2, while those at 0.277, 0.3, and 2.621 keV are exclusive to CKα, OKα, and ClKα, respectively. It is evident that no further impurity peaks were observed. The elements present in the produced Ag nanoparticles were quantified by EDX analysis, which revealed 48.1% for Ag, 19.93% for carbon, 30.66% for oxygen, and 1.31% for Cl. Alkyl chain stabilizers are more likely, given the presence of carbon and oxygen spots in the analyzed samples.[68]

4. CONCLUSIONS

Using $AgNO_3$ as a metal precursor and an extract of PKLs as a reducing and capping agent, this study describes the synthesis of silver nanoparticles at room temperature. First of all, the color of the $AgNO_3$ solution and PKL extract mixture changed from yellow to brown over the reaction time, which confirmed a full-fledged conversion reaction. In the case of characterization after synthesis, UV−visible absorption spectroscopy, FTIR, XRD, FESEM, and EDX were all employed to describe and probe the alteration and nature of silver nanoparticles from Pathor Kuchi leaves. At the outset, the presence of a broad and sharp absorption peak at 443.00 nm in the UV−visible absorption spectrum demonstrates the formation of silver nanoparticles. Moreover, using the Debye−Scherrer equation, the typical crystallite size of the sample was found to be 20.26 nm indicating a nanocrystal. The morphological analysis using FESEM images further revealed that the produced silver nanoparticles are spherical in shape and have a size of 20.625 nm, which is basically very close to the computed value (20.260 nm) from the XRD data using the Debye−Scherrer equation. Furthermore, X-ray diffraction examination confirms that the nanoparticle has an FCC crystalline structure, wherein the (111) plane is the dominant peak and possesses a surface with an atomic arrangement with threefold symmetry, showing an apparent sixfold hexagonal symmetry. In addition, from the elementary analysis by EDX analysis, the percentages of Ag, C, O, and Cl are in 48.1, 19.93, 30.66, and 1.31%, respectively. Finally, the lattice strain (ε), intrinsic stress (σ_S), dislocation density (δ), specific surface area (S), unit cell volume (V_C), and atomic packing fraction (APF) are found at 2.19×10^{-3}, 0.08235 GPa, 3.062045×10^{-3} nm^2, 28.2 m^2/g, 0.067565 nm^3, and 0.74, respectively. However, this paper introduced a new biosynthesis method for Ag NPs, which is significantly faster, cost-effective, and value-generating. The surface area was found to be 1289.50 nm^2, and the ratio of the surface area to volume is 29.6×10^7, which is significantly high. Second, the particle size is 20.626 nm, which shows that the particle size of the crystal is better. Therefore, due to their small crystal size (20.652 nm) as well as catalytic activity, they have potential for various applications in targeted drug delivery, water treatment, materials for solar cells and biosensors, or electronic devices.

■ ASSOCIATED CONTENT

Supporting Information

The Supporting Information is available free of charge at https://pubs.acs.org/doi/10.1021/acsomega.3c01261.

Experimental section, FTIR and NMR, and calculation of surface area and ratio of surface area (PDF)

https://doi.org/10.1021/acsomega.3c01261
ACS Omega 2023, 8, 28133−28142

AUTHOR INFORMATION

Corresponding Authors

Md. Hazrat Ali − *Department of Electrical and Electronic Engineering, European University of Bangladesh (EUB), Dhaka 1216, Bangladesh*; Phone: +8801992008298; Email: ahazrat31@gmail.com

Ajoy Kumer − *Laboratory of Computational Research for Drug Design and Material Science, Department of Chemistry, European University of Bangladesh, Dhaka 1216, Bangladesh*; orcid.org/0000-0001-5136-6166; Phone: +8801770568599; Email: kumarajoy.cu@gmail.com

Authors

Md. Abul Kalam Azad − *Department of Civil Engineering, European University of Bangladesh (EUB), Dhaka 1216, Bangladesh*

K. A. Khan − *Department of Physics, Jagannath University, Dhaka 1100, Bangladesh*

Md. Obaidur Rahman − *Department of Physics, Jahangirnagar University, Dhaka 1342, Bangladesh*

Unesco Chakma − *School of Electronic Science and Engineering, Southeast University, Nanjing 210096, P. R. China; Laboratory of Computational Research for Drug Design and Material Science, Department of Chemistry, European University of Bangladesh, Dhaka 1216, Bangladesh*

Complete contact information is available at: https://pubs.acs.org/10.1021/acsomega.3c01261

Author Contributions

M.H.A. conceived the research project, contributed to modeling and figure creation, wrote the draft of the research, and performed experiments. M.A.K.A., K.A.K., and M.O.R. performed the data preparation, analysis, and plotting of graphs. U.C. contributed to correction, XRD data analysis, and formatting. A.K. wrote the draft and reviewed the work. All authors contributed to the interpretation of the data.

Notes

The authors declare no competing financial interest.

ACKNOWLEDGMENTS

The authors extend their appreciation to the Department of Physics, Jagannath University and Jahangirnagar University, Savar, Dhaka 1342, Bangladesh, for providing facilities to conduct this research.

REFERENCES

(1) Ibrahim, M. Current perspectives of nanoparticles in medical and dental biomaterials. *J. Biomed. Res.* **2012**, *26*, 143−151.

(2) Nair, G. M.; Sajini, T.; Mathew, B. Advanced green approaches for metal and metal oxide nanoparticles synthesis and their environmental applications. *Talanta Open* **2021**, *5*, No. 100080.

(3) Nair, L. S.; Laurencin, C. T. Silver nanoparticles: Synthesis and therapeutic applications. *J. Biomed. Nanotechnol.* **2007**, *3*, 301−316.

(4) You, C.; Han, C.; Wang, X.; Zheng, Y.; Li, Q.; Hu, X.; Sun, H. The progress of silver nanoparticles in the antibacterial mechanism, clinical application and cytotoxicity. *Mol. Biol. Rep.* **2012**, *39*, 9193−9201.

(5) Badmus, J. A.; Oyemomi, S. A.; Adedosu, O. T.; Yekeen, T. A.; Azeez, M. A.; Adebayo, E. A.; Lateef, A.; Badeggi, U. M.; Botha, S.; Hussein, A. A.; Marnewick, J. L. Photo-assisted bio-fabrication of silver nanoparticles using annona muricata leaf extract: Exploring the antioxidant, anti-diabetic, antimicrobial, and cytotoxic activities. *Heliyon* **2020**, *6*, No. e05413.

(6) Jan, H.; Zaman, G.; Usman, H.; Ansir, R.; Drouet, S.; Gigliolo-Guivarc'h, N.; Hano, C.; Abbasi, B. H. Biogenically proficient synthesis and characterization of silver nanoparticles (ag-nps) employing aqueous extract of aquilegia pubiflora along with their in vitro antimicrobial, anti-cancer and other biological applications. *J. Mater. Res. Technol.* **2021**, *15*, 950−968.

(7) Shelley, T. *Nanotechnology: New Promises, New Dangers*; Zed Books, 2006.

(8) Mohajerani, A.; Burnett, L.; Smith, J. V.; Kurmus, H.; Milas, J.; Arulrajah, A.; Horpibulsuk, S.; Kadir, A. Nanoparticles in construction materials and other applications, and implications of nanoparticle use. *Materials* **2019**, *12*, No. 3052.

(9) Mcnamara, K.; Tofail, S. A. Nanoparticles in biomedical applications. *Adv. Phys.: X* **2017**, *2*, 54−88.

(10) Garg, D.; Sarkar, A.; Chand, P.; Bansal, P.; Gola, D.; Sharma, S.; Khantwal, S.; Mehrotra, R.; Chauhan, N.; Bharti, R. K. Synthesis of silver nanoparticles utilizing various biological systems: Mechanisms and applications—a review. *Prog. Biomater.* **2020**, *9*, 81−95.

(11) Uluisik, I.; Karakaya, H. C.; Koc, A. The importance of boron in biological systems. *J. Trace Elem. Med. Biol.* **2018**, *45*, 156−162.

(12) Narayanan, K. B.; Sakthivel, N. Green synthesis of biogenic metal nanoparticles by terrestrial and aquatic phototrophic and heterotrophic eukaryotes and biocompatible agents. *Adv. Colloid Interface Sci.* **2011**, *169*, 59−79.

(13) Jan, H.; Gul, R.; Andleeb, A.; Ullah, S.; Shah, M.; Khanum, M.; Ullah, I.; Hano, C.; Abbasi, B. H. A detailed review on biosynthesis of platinum nanoparticles (ptnps), their potential antimicrobial and biomedical applications. *J. Saudi Chem. Soc.* **2021**, *25*, No. 101297.

(14) Li, J.; Zeng, H.; Zeng, Z.; Zeng, Y.; Xie, T. Promising graphene-based nanomaterials and their biomedical applications and potential risks: A comprehensive review. *ACS Biomater. Sci. Eng.* **2021**, *7*, 5363−5396.

(15) Khan, I.; Saeed, K.; Khan, I. Nanoparticles: Properties, applications and toxicities. *Arabian J. Chem.* **2019**, *12*, 908−931.

(16) Shreyash, N.; Bajpai, S.; Khan, M. A.; Vijay, Y.; Tiwary, S. K.; Sonker, M. Green synthesis of nanoparticles and their biomedical applications: A review. *ACS Appl. Nano Mater.* **2021**, *4*, 11428−11457.

(17) Antognozzi, M.; Bermingham, C. R.; Harniman, R.; Simpson, S.; Senior, J.; Hayward, R.; Hoerber, H.; Dennis, M.; Bekshaev, A.; Bliokh, K.; Nori, F. Direct measurements of the extraordinary optical momentum and transverse spin-dependent force using a nano-cantilever. *Nat. Phys.* **2016**, *12*, 731−735.

(18) Bahrulolum, H.; Nooraei, S.; Javanshir, N.; Tarrahimofrad, H.; Mirbagheri, V. S.; Easton, A. J.; Ahmadian, G. Green synthesis of metal nanoparticles using microorganisms and their application in the agrifood sector. *J. Nanobiotechnol.* **2021**, *19*, No. 86.

(19) Kamboj, A.; Saluja, A. Bryophyllum pinnatum (lam.) kurz.: Phytochemical and pharmacological profile: A review. *Pharmacogn. Rev.* **2009**, *3*, No. 364.

(20) Tomita, M.; Murakami, M. High-temperature superconductor bulk magnets that can trap magnetic fields of over 17 tesla at 29 k. *Nature* **2003**, *421*, 517−520.

(21) Sur, U. K.Biosynthesis of Metal Nanoparticles and Graphene. In *Advanced Surface Engineering Materials*; John Wiley & Sons, 2016; pp 241−295.

(22) Han, X.; P, Tory L. Lemongrass (cymbopogon flexuosus) essential oil demonstrated anti-inflammatory effect in pre-inflamed human dermal fibroblasts. *Biochim. Open* **2017**, *4*, 107−111.

(23) Pouyan, S.; Kafshdouzan, K.; Jebelli, A. Synergistic effect of cinnamomum camphora and origanum vulgare essential oils against bla ctx-m producing escherichia coli isolated from poultry colibacillosis. *J. Med. Bacteriol.* **2021**, 20−29.

(24) Islas, J. F.; Acosta, E.; Zuca, G.; Delgado-Gallegos, J. L.; Moreno-Treviño, M. G.; Escalante, B.; Moreno-Cuevas, J. E. An overview of neem (azadirachta indica) and its potential impact on health. *J. Funct. Foods* **2020**, *74*, No. 104171.

(25) Surjushe, A.; Vasani, R.; Saple, D. G. Aloe vera: A short review. *Indian J. Dermatol.* **2008**, *53*, 163−166.
(26) Al-Jobouri, A. H. A. Studying some the functional properties of tamarind tamarindus indica l. Mucilage. *Al-Qadisiyah J. Agric. Sci.* **2020**, *10*, 304−307.
(27) Phochantachinda, S.; Chatchaisak, D.; Temviriyanukul, P.; Chansawang, A.; Pitchakarn, P.; Chantong, B. Ethanolic fruit extract of emblica officinalis suppresses neuroinflammation in microglia and promotes neurite outgrowth in neuro2a cells. *Evidence-Based Complementary Altern. Med.* **2021**, *2021*, 1−16.
(28) El-Seedi, H. R.; El-Shabasy, R. M.; Khalifa, S. A.; Saeed, A.; Shah, A.; Shah, R.; Iftikhar, F. J.; Abdel-Daim, M. M.; Omri, A.; Hajrahand, N. H.; et al. Metal nanoparticles fabricated by green chemistry using natural extracts: Biosynthesis, mechanisms, and applications. *RSC Adv.* **2019**, *9*, 24539−24559.
(29) Chokkareddy, R.; Redhi, G. G. Green synthesis of metal nanoparticles and its reaction mechanisms. *Green Met. Nanopart.* **2018**, 113−139.
(30) Fatehbasharzad, P.; Fatehbasharzad, P.; Sillanpää, M.; Shamsi, Z. Investigation of bioimpacts of metallic and metallic oxide nanostructured materials: Size, shape, chemical composition, and surface functionality: A review. *Part. Part. Syst. Charact.* **2021**, *38*, No. 2100112.
(31) Behzad, F.; Naghib, S. M.; kouhbanani, M. A. J.; Tabatabaei, S. N.; Zare, Y.; Rhee, K. Y. An overview of the plant-mediated green synthesis of noble metal nanoparticles for antibacterial applications. *J. Ind. Eng. Chem.* **2021**, *94*, 92−104.
(32) Nejati, K.; Dadashpour, M.; Gharibi, T.; Mellatyar, H.; Akbarzadeh, A. Biomedical applications of functionalized gold nanoparticles: A review. *J. Cluster Sci.* **2021**, *33*, 1−16.
(33) Chavali, M. S.; Nikolova, M. P. Metal oxide nanoparticles and their applications in nanotechnology. *SN Appl. Sci.* **2019**, *1*, No. 607.
(34) Khan, Y.; Sadia, H.; Shah, S. Z. A.; Khan, M. N.; Shah, A. A.; Ullah, N.; Ullah, M. F.; Bibi, H.; Bafakeeh, O. T.; Khedher, N. B.; et al. Classification, synthetic, and characterization approaches to nanoparticles, and their applications in various fields of nanotechnology: A review. *Catalysts* **2022**, *12*, No. 1386.
(35) Khayal, A.; Dawane, V.; Amin, M. A.; Tirth, V.; Yadav, V. K.; Algahtani, A.; Khan, S. H.; Islam, S.; Yadav, K. K.; Jeon, B.-H. Advances in the methods for the synthesis of carbon dots and their emerging applications. *Polymers* **2021**, *13*, No. 3190.
(36) Assad, H.; Kaya, S.; Kumar, P. S.; Vo, D.-V.N.; Sharma, A.; Kumar, A. Insights into the role of nanotechnology on the performance of biofuel cells and the production of viable biofuels: A review. *Fuel* **2022**, *323*, No. 124277.
(37) Khan, K. A.; Rasel, S. R.; Ohiduzzaman, M. Homemade pkl electricity generation for use in dc fan at remote areas. *Microsyst. Technol.* **2019**, *25*, 4529−4536.
(38) Khan, K. A.; Mamun, M. A.; Ibrahim, M.; Hasan, M.; Ohiduzzaman, M.; Obaydullah, A. K. M.; Wadud, M. A.; Shajahan, M. Pkl electrochemical cell: Physics and chemistry. *SN Appl. Sci.* **2019**, *1*, No. 1335.
(39) Zare-Bidaki, M.; Mohammadparast-Tabas, P.; Peyghambari, Y.; Chamani, E.; Siami-Aliabad, M.; Mortazavi-Derazkola, S. Photochemical synthesis of metallic silver nanoparticles using pistacia khinjuk leaves extract (pkl@ agnps) and their applications as an alternative catalytic, antioxidant, antibacterial, and anticancer agents. *Appl. Organomet. Chem.* **2022**, *36*, No. e6478.
(40) Paul, B.; Khan, K. A.; Paul, M. Study the Impact of Green Synthesized Silver Nanoparticles on Bio-Voltaic Cell. In *Lecture Notes in Electrical Engineering*; Springer, 2022; pp 455−465.
(41) Ruby; Aryan; Mehata, M. S. Surface plasmon resonance allied applications of silver nanoflowers synthesized from breynia vitis-idaea leaf extract. *Dalton Trans.* **2022**, *51*, 2726−2736.
(42) Lin, H.; Huang, C.; Li, W.; Ni, C.; Shah, S.; Tseng, Y. Size dependency of nanocrystalline tio2 on its optical property and photocatalytic reactivity exemplified by 2-chlorophenol. *Appl. Catal., B* **2006**, *68*, 1−11.
(43) Aziz, S. B.; Hussein, G.; Brza, M. A.; Mohammed, S. J.; Abdulwahid, R. T.; Saeed, S. R.; Hassanzadeh, A. Fabrication of interconnected plasmonic spherical silver nanoparticles with enhanced localized surface plasmon resonance (lspr) peaks using quince leaf extract solution. *Nanomaterials* **2019**, *9*, No. 1557.
(44) Ren, W.; Lin, G.; Clarke, C.; Zhou, J.; Jin, D. Optical nanomaterials and enabling technologies for high-security-level anticounterfeiting. *Adv. Mater.* **2020**, *32*, No. 1901430.
(45) Abdellatif, A. A. H.; Alhathloul, S. S.; Aljohani, A. S.; Maswadeh, H.; Abdallah, E. M.; Musa, K. H.; El Hamd, M. A. Green synthesis of silver nanoparticles incorporated aromatherapies utilized for their antioxidant and antimicrobial activities against some clinical bacterial isolates. *Bioinorg. Chem. Appl.* **2022**, *2022*, 1−14.
(46) Kainz, M. P.; Legenstein, L.; Holzer, V.; Hofer, S.; Kaltenegger, M.; Resel, R.; Simbrunner, J. Gidind: An automated indexing software for grazing-incidence x-ray diffraction data. *J. Appl. Crystallogr.* **2021**, *54*, 1256−1267.
(47) Guzmán, K.; Kumar, B.; Vallejo, M. J.; Grijalva, M.; Debut, A.; Cumbal, L. Ultrasound-assisted synthesis and antibacterial activity of gallic acid-chitosan modified silver nanoparticles. *Prog. Org. Coat.* **2019**, *129*, 229−235.
(48) Dawood, A.; Moosa, A.; Radhi, M. Green synthesis of silver nanoparticles decorated with exfoliated graphite nanocomposites. *Egypt. J. Chem.* **2022**, *65*, 651−659.
(49) Vernasqui, L. G.; Kawata, B. A.; Sardinha, A. F.; Rodrigo, M. A.; Ferreira, N. G. Achievement and electrochemical responsiveness of advanced boron-doped ultrananocrystalline diamond on highly ordered titanium dioxide nanotubes. *Diamond Relat. Mater.* **2022**, *121*, No. 108793.
(50) Chirumamilla, P.; Dharavath, S. B.; Taduri, S. Eco-friendly green synthesis of silver nanoparticles from leaf extract of solanum khasianum: Optical properties and biological applications. *Appl. Biochem. Biotechnol.* **2022**, *195*, 352−368.
(51) Kanimozhi, S.; Durga, R.; Sabithasree, M.; Kumar, A. V.; Sofiavizhimalar, A.; Kadam, A. A.; Rajagopal, R.; Sathya, R.; Azelee, N. I. W. Biogenic synthesis of silver nanoparticle using cissus quadrangularis extract and its invitro study. *J. King Saud Univ. - Sci.* **2022**, *34*, No. 101930.
(52) Oves, M.; Rauf, M. A.; Aslam, M.; Qari, H. A.; Sonbol, H.; Ahmad, I.; Zaman, G. S.; Saeed, M. Green synthesis of silver nanoparticles by conocarpus lancifolius plant extract and their antimicrobial and anticancer activities. *Saudi J. Biol. Sci.* **2022**, *29*, 460−471.
(53) Chandrasekharan, S.; Chinnasamy, G.; Bhatnagar, S. Sustainable phyto-fabrication of silver nanoparticles using gmelina arborea exhibit antimicrobial and biofilm inhibition activity. *Sci. Rep.* **2022**, *12*, No. 156.
(54) Chérif, I.; Dkhil, Y. O.; Smaoui, S.; Elhadef, K.; Ferhi, M.; Ammar, S. X-ray diffraction analysis by modified scherrer, williamson−hall and size−strain plot methods of zno nanocrystals synthesized by oxalate route: A potential antimicrobial candidate against foodborne pathogens. *J. Cluster Sci.* **2022**, *34*, 623−638.
(55) Manopradha, N.; Gowri, S.; Rama, S.; Selvaraju, K.; Kirubavathi, K. Nucleation kinetics, williamson-hall analysis, hardness and dielectric properties of pyridine-2-carboxylictrichloroacetate single crystals. *Phys. B* **2022**, *624*, No. 413397.
(56) Yousefi, S.; Ghasemi, B.; Nikolova, M. P. Morpho/opto-structural characterizations and xrd-assisted estimation of crystallite size and strain in mgo nanoparticles by applying williamson−hall and size−strain techniques. *J. Cluster Sci.* **2022**, *33*, 2197−2207.
(57) Ali, A.; Chiang, Y. W.; Santos, R. M. X-ray diffraction techniques for mineral characterization: A review for engineers of the fundamentals, applications, and research directions. *Minerals* **2022**, *12*, No. 205.
(58) Maurya, P.; Kota, N.; Gibmeier, J.; Wanner, A.; Roy, S. Review on study of internal load transfer in metal matrix composites using diffraction techniques. *Mater. Sci. Eng.: A* **2022**, *840*, No. 142973.

https://doi.org/10.1021/acsomega.3c01261
ACS Omega 2023, 8, 28133−28142

(59) Kirk, S. R.; Jenkins, S. Beyond energetic and scalar measures: Next generation quantum theory of atoms in molecules. *WIRES Comput. Mol. Sci.* **2022**, *12*, No. e1611.
(60) Romero-Resendiz, L.; El-Tahawy, M.; Zhang, T.; Rossi, M. C.; Marulanda-Cardona, D. M.; Yang, T.; Amigó-Borrás, V.; Huang, Y.; Mirzadeh, H.; Beyerlein, I. J.; et al. Heterostructured stainless steel: Properties, current trends, and future perspectives. *Mater. Sci. Eng., R* **2022**, *150*, No. 100691.
(61) Li, X.-N.; Wang, X.-M.; Bai, X.; Liu, Y.-Y.; Gui, T.; Wang, X.-Q.; Xue, Z.-Y.; Wen, J.K. Densification mechanism during hot-pressing of single-phase zirconium boride powders with different dislocation density. *Ceram. Int.* **2022**, *48*, 19305−19313.
(62) Gandhad, S. S.; Jeergal, P. R.; Veena, E.; Hublikar, L.; Horakeri, L. D.; Mathad, S. N.; Patil, S. R. Synthesis and characterization of silver nanoparticles using green route. *Int. J. Adv. Sci. Eng.* **2022**, *8*, No. 2252.
(63) Zhou, W.; Cao, Y.; Zhao, H.; Li, Z.; Feng, P.; Feng, F. Fractal analysis on surface topography of thin films: A review. *Fractal Fractional* **2022**, *6*, No. 135.
(64) Faraj, R. H.; Ahmed, H. U.; Rafiq, S.; Sor, N.H.; Ibrahim, D. F.; Qaidi, S. M. A. Performance of self-compacting mortars modified with nanoparticles: A systematic review and modeling. *Cleaner Mater.* **2022**, *4*, No. 100086.
(65) Hosseini, S. S.; Jebelli, A.; Vandghanooni, S.; Jahanban-Esfahlan, A.; Baradaran, B.; Amini, M.; Bidar, N.; de la Guardia, M.; Mokhtarzadeh, A.; Eskandani, M. Perspectives and trends in advanced DNA biosensors for the recognition of single nucleotide polymorphisms. *Chem. Eng. J.* **2022**, *441*, No. 135988.
(66) Altorbaq, A. S.; Krauskopf, A. A.; Wen, X.; Pérez-Camargo, R. A.; Su, Y.; Wang, D.; Müller, A. J.; Kumar, S. K. Crystallization kinetics and nanoparticle ordering in semicrystalline polymer nanocomposites. *Prog. Polym. Sci.* **2022**, *128*, No. 101527.
(67) Nasrollahzadeh, M. Green synthesis and catalytic properties of palladium nanoparticles for the direct reductive amination of aldehydes and hydrogenation of unsaturated ketones. *New J. Chem.* **2014**, *38*, 5544−5550.
(68) Ramamoorthy, R. K.; Soulantica, K.; Del Rosal, I.; Arenal, R.; Decorse, P.; Piquemal, J.-Y.; Chaudret, B.; Poteau, R.; Viau, G. Ruthenium icosahedra and ultrathin platelets: The role of surface chemistry on the nanoparticle structure. *Chem. Mater.* **2022**, *34*, 2931−2944.

https://doi.org/10.1021/acsomega.3c01261
ACS Omega 2023, 8, 28133−28142